Check for updates

Advanced Functional Materials

ADVANCED FUNCTIONAL MATERIALS
www.afm-journal.de

RESEARCH ARTICLE OPEN ACCESS

In-Situ Solution Complexation for n-Type Surface-Energetics Reconstruction in 2.0 eV Ultra-Wide-Bandgap Perovskite Solar Cells

Saemon Yoon[1] | Han-Gyun Lim[2] | Jinyoung Kim[3] | Gyu Min Kim[4] | Seojun Lee[1] | Jun Ryu[1] | SungWon Cho[1] | Jincheol Kim[5] | Hyosung Choi[6] | Jung Sang Cho[7,8] | Jongsung Park[9] | Dong-Won Kang[2]

[1]Department of Smart Cities, Chung-Ang University, Seoul, Republic of Korea | [2]Department of Energy Systems Engineering, Chung-Ang University, Seoul, Republic of Korea | [3]Department of Chemical and Biomolecular Engineering, Sogang University, Seoul, Republic of Korea | [4]Department of Chemical Engineering, Hankyong National University, Anseong, Republic of Korea | [5]School of Engineering, Macquarie University, Sydney, New South Wales, Australia | [6]Department of Chemistry, Research Institute for Natural Sciences, and Research Institute for Convergence of Basic Science, Hanyang University, Seoul, Republic of Korea | [7]Department of Engineering Chemistry, Chungbuk National University, Chungbuk, Republic of Korea | [8]Advanced Energy Research Institute, Chungbuk National University, Cheongju, Chungbuk, Republic of Korea | [9]Department of Energy Engineering, Department of Energy System Engineering, Gyeongsang National University, Jinju, Gyeongnam, Republic of Korea

Correspondence: Jung Sang Cho (jscho@cbnu.ac.kr) | Jongsung Park (j.park@gnu.ac.kr) | Dong-Won Kang (kangdwn@cau.ac.kr)

Received: 14 December 2025 | **Revised:** 15 February 2026 | **Accepted:** 18 March 2026

Keywords: perovskite tandem solar cell | proton transfer | surface reconstruction | ultra-wide-bandgap perovskite

ABSTRACT

Ultra-wide-bandgap (UWBG) perovskites (>2.0 eV) are essential for high-efficiency triple-junction tandem solar cells but suffer from photo-induced phase segregation and open-circuit voltage (V_{OC}) deficits arising from surface defects and energetic misalignment. Here, we report an in situ solution complexation (ISC) strategy to reconstruct the surface of 2.0 eV perovskites. By exploiting a proton transfer reaction between phenethylammonium chloride and ethylenediamine, we activate the passivation agents to selectively deplete unstable surface iodine clusters and eliminate metallic lead defects. This chemical reconstruction induces a degenerate-like n-type surface with pronounced downward band bending, simultaneously forming a robust hole-blocking barrier and enabling efficient electron extraction via an Ohmic tunneling contact. Consequently, the ISC-treated 2.0 eV single-junction device achieves a power conversion efficiency (PCE) of 15.7% with a high V_{OC} of 1.41 V and a fill factor of 0.84, while exhibiting superior photostability by suppressing phase segregation. Leveraging this UWBG top cell together with a 1.5 eV perovskite bottom cell, we further demonstrate a monolithic all-perovskite tandem solar cell delivering a PCE of 24.2% with a V_{OC} of 2.58 V. This work provides a practical pathway to minimize voltage losses and stabilize UWBG perovskites, advancing perovskite tandems toward perovskite/perovskite/Si triple-junction architecture.

1 | Introduction

Perovskite solar cells (PSCs) have significantly transformed the field of photovoltaics, achieving single-junction power conversion efficiencies (PCEs) surpassing 27%, while perovskite/silicon tandem devices have exceeded 34%, approaching the theoretical Shockley-Queisser (S-Q) limit of single-junction devices [1–3]. To surpass this limit, current research is progressing toward triple-junction architectures, which theoretically can attain efficiencies greater than 50% [4–6]. A critical component in realizing such high efficiencies is the development of high-performance ultra-wide-bandgap (UWBG) perovskite top cells with bandgaps

This is an open access article under the terms of the Creative Commons Attribution License, which permits use, distribution and reproduction in any medium, provided the original work is properly cited.

© 2026 The Author(s). *Advanced Functional Materials* published by Wiley-VCH GmbH

above 2.0 eV [7–13]. However, the performance of these UWBG absorbers is significantly hindered by a substantial open-circuit voltage (V_{OC}) deficit and limited operational stability. These issues primarily arise from photo-induced halide segregation, wherein mixed-halide perovskites undergo demixing into iodide-rich, lower-bandgap domains under illumination, as well as from high densities of non-radiative recombination centers located at grain boundaries and interfaces [14–16].

Addressing these challenges necessitates precise control over the crystallization kinetics and surface energetics. Prior studies have concentrated on A-site cation engineering, such as incorporating rubidium (Rb) or cesium (Cs), to induce lattice distortion and increase the ion migration barrier, thereby mitigating phase segregation [9]. Other approaches have employed pseudo-halides (e.g., OCN, SCN) or Lewis base additives to regulate film growth and homogenize halide distribution [10]. Despite improvements in bulk film quality, the perovskite surface remains a critical bottleneck. Conventional surface passivation using bulky ammonium salts, such as phenethylammonium chloride (PEACl), typically forms insulating 2D layers that impede charge extraction, creating a trade-off between V_{OC} and fill factor (FF) [17–19]. In contrast, the use of strong chelating agents often causes excessive surface etching and structural degradation [20–22]. Consequently, a strategy that simultaneously reconstructs defective surfaces and optimizes interfacial energy alignment without compromising carrier transport has yet to be realized.

In this study, we introduce a reactive passivator engineering strategy, termed In Situ Solution Complexation (ISC), to reconstruct the surface of 2.0 eV UWBG perovskites. Rather than employing physical blending, this method exploits a proton transfer reaction between PEACl and ethylenediamine (EDA) within the surface treatment solution. This reaction activates the bulky cations into reactive free amines while converting the chelating agent into a non-destructive stabilizer. Our findings indicate that this approach selectively removes unstable surface iodine clusters and eliminates metallic lead (Pb^0) defects, resulting in a robust, bromine-enriched surface. Importantly, ultraviolet photoelectron spectroscopy (UPS) and Kelvin probe force microscopy (KPFM) analyses reveal that this chemical reconstruction induces a degenerate-like n-type surface character accompanied by pronounced downward band bending. This energetic configuration serves as an effective hole-blocking barrier while establishing an Ohmic tunneling contact for efficient electron extraction.

By leveraging this strategy, we achieved a 2.0 eV single-junction PSC with a PCE of 15.7%, a high V_{OC} of 1.41 V, and an FF of 0.842, thereby overcoming the conventional trade-off between passivation and charge transport. The device also demonstrated enhanced photostability, retaining over 85% of its initial efficiency after 100 h of continuous maximum power point (MPP) tracking, which is attributed to the suppression of phase segregation. Furthermore, to demonstrate direct relevance to triple-junction photovoltaics, we integrate the 2.0 eV UWBG subcell as the top junction with a 1.5 eV perovskite middle cell in a monolithic configuration, delivering a PCE of 24.2% together with an ultrahigh V_{OC} of 2.58 V. Such a high-voltage 2.0/1.5 eV top–middle platform provides a key technological foundation for perovskite/perovskite/Si triple-junction architecture, where the summed photovoltage and interfacial phase stability are decisive.

2 | Results and Discussion

To elucidate the chemical origin of the ISC strategy, we investigated the interaction between PEACl and EDA within the solution. The reaction is hypothesized to involve a proton transfer, where the lone pair of EDA abstracts a proton from the ammonium group of PEA^+, activating it into a reactive free amine (NH_2) while converting EDA into a stable cation predominantly monoprotonated $EDAH^+$ under our near-equimolar ISC formulation, with a possible minor contribution from $EDAH_2^{2+}$ (Figure 1a). This chemical switching is corroborated by UV–vis absorption spectroscopy (Figure 1c). The distinct bathochromic shift of the absorption onset from 258 nm (PEACl solution) to 279 nm (ISC solution) is consistent with an altered electronic environment upon in situ solution complexation [23–25]. Importantly, to directly verify the proposed proton-transfer reaction and correlate the ISC solution with the expected product species, we performed ^{1}H NMR measurements (DMSO-d_6) for PEACl, EDA, their mixture (ISC), and PEA (Figure S1). In the mixed solution, the characteristic ammonium resonance of PEACl (δ 8.26–8.22 ppm, NH_3^+) is markedly suppressed, accompanied by the appearance of PEA-like aliphatic resonances in the 2.8–2.7 ppm region (δ 2.84, 2.73, and 2.68 ppm) and a trace exchangeable proton signal at δ ≈4.95 ppm, indicating the formation of protonated EDA species ($EDAH^+$ and/or partially $EDAH_2^{2+}$). These NMR results provide direct spectroscopic evidence for proton-transfer-mediated activation in the ISC solution. Accordingly, the consistent changes in surface chemistry, electronic structure, and device performance presented in the following sections strongly support a proton-transfer-mediated activation mechanism.

Subsequently, we investigated the influence of this chemical activation on the crystallographic evolution using X-ray diffraction (XRD). As shown in Figure 1d and the full-range patterns in Figure S2, the control film exhibits a typical 3D perovskite phase. Notably, the film treated with neat PEACl displays a distinct low-angle peak at 5.2°, assigned to the formation of a layered 2D perovskite phase ($n = 1$ or $n = 2$) [26, 27]. This observation aligns with the surface schematic in Figure 1b, where bulky PEA cations, lacking sufficient kinetic energy for penetration, aggregate randomly on the surface to form an insulating barrier. In stark contrast, the ISC-treated film shows a complete suppression of this 2D peak. Furthermore, grazing-incidence XRD (GI-XRD) patterns (Figure S3) collected at a fixed incident angle ($\omega = 0.5°$) while varying the sample tilt angle ($\psi = 0–40°$) show no detectable secondary diffraction peaks or pronounced peak broadening across all samples, indicating that the bulk perovskite crystallographic framework is largely preserved after the surface treatments.

The chemical nature of this surface reconstruction was probed by high-resolution X-ray photoelectron spectroscopy (XPS) (Figure 1e). The Pb 4f spectra reveal that the control film possesses a noticeable shoulder at lower binding energy (136.4 eV), indicative of metallic lead (Pb^0) defects arising from surface iodine deficiency [28–30]. We note that X-ray irradiation can induce iodide loss and Pb° formation in halide perovskites during XPS measurements. Therefore, all spectra in this work were collected under identical acquisition and exposure conditions for a consistent relative comparison. Notably, the EDA-only treatment exacerbates this issue, showing a substantial Pb^0

16163028, 0, Downloaded from https://advanced.onlinelibrary.wiley.com/doi/10.1002/adfm.202532139 by Chungbuk National University, Wiley Online Library on [26/03/2026]. See the Terms and Conditions (https://onlinelibrary.wiley.com/terms-and-conditions) on Wiley Online Library for rules of use; OA articles are governed by the applicable Creative Commons License

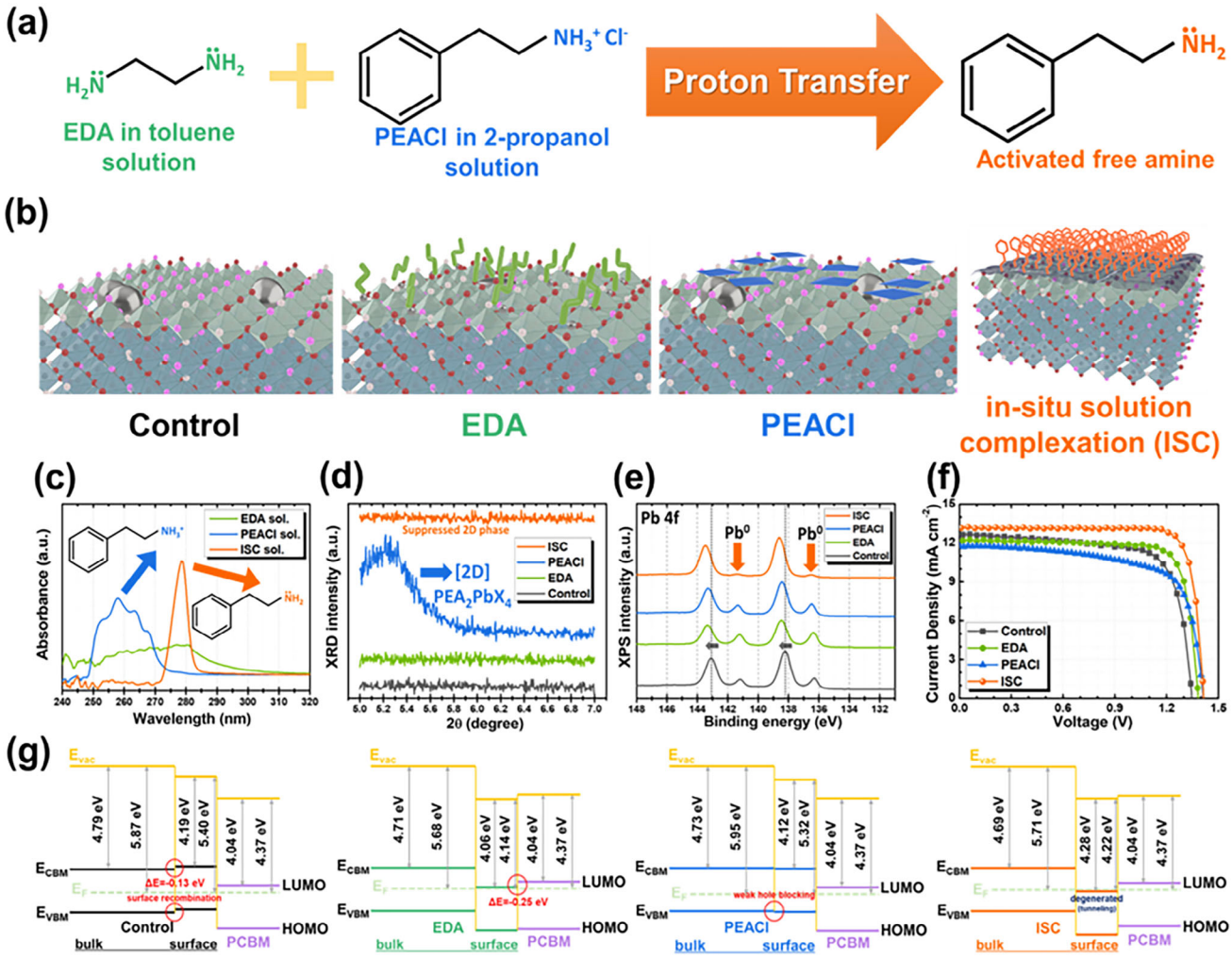

FIGURE 1 | (a) Schematic illustration of the proposed proton transfer reaction between PEACl and EDA, and (b) comparison of the resulting surface evolution. (c) UV–vis absorption spectra of the surface treatment solutions. (d) XRD patterns and (e) high-resolution Pb 4f XPS spectra of Control, EDA-, PEACl-, and ISC-treated films. (f) *J-V* characteristics of the corresponding devices. (g) Energy band diagrams illustrating the ISC-induced modification of surface electronic structure.

signal, which we attribute to the excessive etching of surface halides by the strong chelating nature of neutral EDA, leading to localized surface halide depletion and structural deterioration as depicted in Figure 1b, while the GI-XRD patterns exhibit no discernible bulk structural degradation (Figure S3), supporting preserved bulk crystallography. Conversely, the ISC treatment considerably eliminates the Pb^0 defects. Since all measurements were performed under identical X-ray exposure conditions, this sharp contrast confirms that the metallic signals observed in the EDA sample are intrinsic to chemical etching rather than artifacts of X-ray beam damage. Mechanistically, the ISC-derived amine species, comprising protonated EDA ($EDAH^+$ and/or partially $EDAH_2^{2+}$) and deprotonated PEA-like free-base species, collectively establish a non-destructive stabilization environment. This strategy eliminates Pb^0 defects by suppressing the aggressive halide etching associated with neutral EDA while reinforcing Pb-N coordination, as evidenced by the disappearance of the Pb^0 signal and the positive binding-energy shift of Pb^{2+} in surface-sensitive XPS. Simultaneously, the cooperative interaction between these species facilitates a selective surface reconstruction, wherein chemically unstable iodine-related surface species are mitigated in favor of a more robust bromine-enriched and chlorine-anchored surface stoichiometry.

Moreover, the main Pb^{2+} peak in the ISC film shifts to a higher binding energy by 0.07 eV compared to the control. This positive shift signifies increased electron withdrawal from Pb, confirming the formation of robust coordinate bonds between the under-coordinated surface Pb and the nitrogen lone pairs of the activated PEA/EDA complex [31]. Quantitative surface/bulk-like atomic concentration analysis (Figure S4) further reveals that the ISC treatment selectively depletes the unstable surface iodine (from 14.5% to 5.8%) while maintaining a bromine-rich and chlorine-anchored surface, thereby eliminating the initiation sites for phase segregation.

We assessed the impact of these surface modifications on the photovoltaic performance of 2.0 eV single-junction devices with a p-i-n architecture of ITO/NiO_x/Me-4PACz/$FA_{0.85}Cs_{0.15}PbIBr_{1.8}Cl_{0.2}$/surface treatment/PCBM/BCP/Ag. The current density-voltage (*J-V*) curves and corresponding photovoltaic parameters are

16163028, 0, Downloaded from https://advanced.onlinelibrary.wiley.com/doi/10.1002/adfm.202532139 by Chungbuk National University, Wiley Online Library on [26/03/2026]. See the Terms and Conditions (https://onlinelibrary.wiley.com/terms-and-conditions) on Wiley Online Library for rules of use; OA articles are governed by the applicable Creative Commons License

TABLE 1 | Photovoltaic parameters of the 2.0 eV PSCs with different surface treatments.

Device	V_{OC} (V)	J_{SC} (mA cm^{-2})	FF	PCE (%)
Control	1.35	12.70	0.729	12.5
EDA	1.38	12.24	0.802	13.6
PEACl	1.41	11.78	0.692	11.5
ISC	1.41	13.17	0.842	15.7

summarized in Figure 1f and Table 1. The control device exhibits a limited PCE of 12.5% with a low FF of 0.729, suffering from severe hysteresis. The PEACl-only device shows an even lower FF of 0.692, which is directly attributed to the charge transport barrier formed by the insulating 2D aggregates identified in the XRD analysis. Such a passivation–transport trade-off is particularly pronounced in UWBG perovskites, where the formation of non-uniform, island-like 2D-rich domains can negate the benefits of defect passivation by introducing significant interfacial extraction barriers. The ISC strategy effectively bypasses this limitation by achieving a molecularly reconstructed surface that balances effective passivation with efficient charge transport. Although the EDA treatment improves the V_{OC} to 1.38 V, its performance is constrained by the surface damage and metallic defects. Strikingly, the ISC-treated device achieves a champion PCE of 15.7%, with a significantly enhanced V_{OC} of 1.41 V and a record-high FF of 0.842. The short-circuit current density (J_{SC}) also increases to 13.17 mA cm^{-2}. This simultaneous enhancement in all parameters indicates that the ISC strategy successfully resolves the trade-off between defect passivation and charge extraction. To directly verify whether the PEA species alone can account for such improvements, we performed additional control experiments using PEA-only post-treatments (0.75–6.0 mM) under identical processing conditions. Notably, the PEA-only treatment failed to reproduce the superior ISC-level performance, yielding significantly lower FF and PCE across all tested concentrations (Figure S5 and Table S1). These results clearly distinguish the ISC effect from simple amine passivation and confirm the unique cooperative role of the ISC-derived amine species in achieving high-performance 2.0 eV perovskite solar cells.

To elucidate the physical origin of this performance enhancement, energy band diagrams (Figure 1g) were constructed based on UPS (Figure S6) and Tauc plot analyses (Figure S7). To avoid ambiguity, the UPS-derived spectral shifts were deconvoluted into the work function (WF), derived from the secondary electron cutoff, and EF-VBM component, from the valence band onset (Figure S6 and Table S2). Notably, while both EDA and ISC treatments exhibit significant WF reductions (ΔWF $\approx$1.2 eV), they also show a substantial increase in the surface EF-VBM from 0.79 eV (control) to 1.92 eV (EDA) and 2.06 eV (ISC). This large shift in EF-VBM is the primary origin of the $\approx$1 eV-scale spectral shift observed, indicating a pronounced surface-local band bending and electron accumulation that drives the degenerate-like n-type character. The control film shows an upward band bending at the surface, generating an extraction barrier for electrons. Although EDA-treated film induces a WF reduction, it introduces an energetic barrier at the electron transport layer (ETL) interface, hindering efficient charge collection. While the PEACl-treated film retains a p-type surface character with a flat band alignment, offering no beneficial field-effect passivation against hole recombination, which explains its limited of low FF. In contrast, the ISC treatment induces a dramatic reconstruction of the surface energetics. It reduces the WF and shifts the Fermi level above the conduction band minimum, creating a degenerate-like n-type surface. Here, the term "degenerate-like n-type surface" refers to a quasi-degenerate electron accumulation layer localized near the perovskite surface, where the Fermi level approaches or slightly exceeds the conduction band minimum. Importantly, the term "degenerate-like n-type surface" is used here to emphasize that this electronic reconstruction is confined to a surface-localized region with nanometer-scale thickness, rather than representing bulk degeneracy throughout the perovskite film. In this context, the effective degeneracy is device-relevant, as it enables tunneling-assisted Ohmic electron extraction across the perovskite/ETL interface without requiring a high bulk carrier concentration. This pronounced n-type character induces a significant downward band bending, which functions as a robust hole-blocking barrier to suppress surface recombination. Simultaneously, the degenerate-like surface enables efficient electron extraction via an Ohmic tunneling contact, overcoming the energetic offset. This ideal energetic landscape, combined with the removal of surface traps, is the primary driver for the superior V_{OC} and FF in the ISC-treated devices.

To examine the surface microstructure and electrical uniformity, atomic force microscopy (AFM) and KPFM analyses were conducted (Figure 2a). KPFM measurements were performed in lift mode to minimize topography-potential cross-talk. All samples were measured using identical probe type and scanning parameters, and topography and surface potential were acquired sequentially under the same conditions. The control film exhibits a rough surface with an RMS roughness (R_q) of 21.2 nm. The PEACl and EDA treatments reduce the roughness to 14.6 and 15.3 nm, respectively. However, the KPFM potential map of the PEACl-treated film displays distinct potential dips corresponding to the physical aggregates. These local variations are further evidenced by the fluctuating contact potential difference (CPD) line profiles (Figure 2b). Such inhomogeneity indicates a disordered surface dipole distribution, which can act as scattering centers for charge carriers. In contrast, the ISC-treated film shows compact morphology with the lowest R_q of 12.1 nm. Correspondingly, the KPFM map demonstrates a highly uniform surface potential. Notably, the average CPD value of the ISC film increases to 1.81 V compared to 0.67 V for the control. This positive shift spatially corroborates the WF reduction observed in UPS and confirms the formation of a uniform n-type surface across the film. It should be noted that the observed CPD increase reflects a modification of surface electrostatics rather than bulk doping, supporting the formation of a surface-confined electron accumulation layer. Such a localized electronic reconstruction is sufficient to govern interfacial charge extraction and recombination dynamics, particularly under operating conditions relevant to photovoltaic devices.

Phase stability and recombination distribution were further visualized through confocal photoluminescence (PL) mapping (Figure 2c). Under continuous illumination for 100 s, the control and EDA-treated films develop characteristic worm-like domains.

16163028, 0, Downloaded from https://advanced.onlinelibrary.wiley.com/doi/10.1002/adfm.202532139 by Chungbuk National University, Wiley Online Library on [26/03/2026]. See the Terms and Conditions (https://onlinelibrary.wiley.com/terms-and-conditions) on Wiley Online Library for rules of use; OA articles are governed by the applicable Creative Commons License

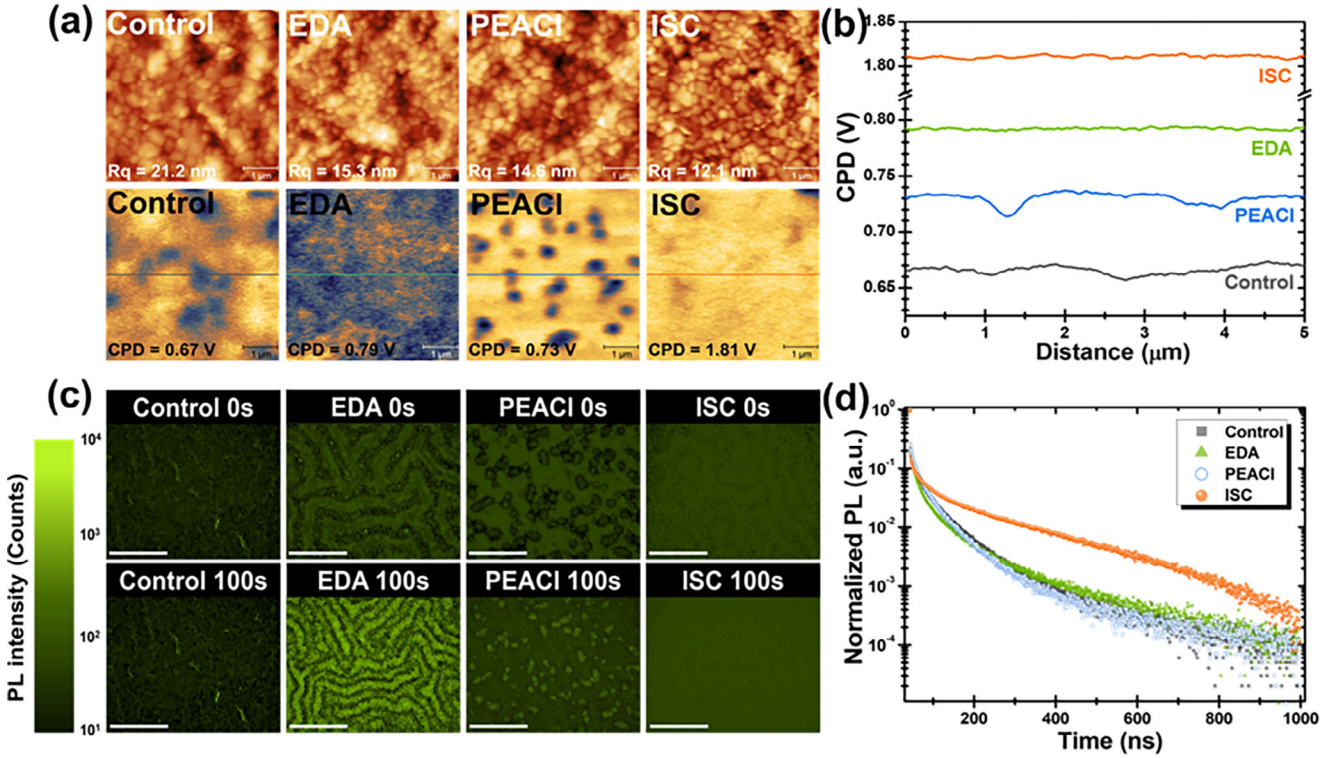

FIGURE 2 | (a) AFM topography and KPFM surface potential maps and (b) extracted cross-sectional CPD line profiles of control, EDA-, PEACl-, and ISC-treated perovskite films. (c) PL mapping images before and after light soaking, and (d) TRPL decay curves of the corresponding perovskite films (Scale bar = 5 μm).

The PEACl-treated film shows localized emission hot spots, likely originating from the aggregated 2D phases. Notably, while the AFM topography appears comparable across all samples, the PL mapping reveals distinct electronic heterogeneities in the PEACl-only case. These localized emission hot spots are consistent with spatially aggregated 2D-rich domains, where excitonic confinement and energy funneling yield locally intensified emission. Conversely, the ISC-treated film maintains a uniform and intense emission without such segregation features, confirming that the chemical reconstruction effectively suppresses uncontrolled phase aggregation and immobilizes halide ions. These patterns are attributed to photo-induced phase segregation where iodide-rich low-bandgap clusters act as radiative recombination centers [32, 33]. The PEACl-treated film shows localized bright spots, likely originating from the aggregated 2D phases. These localized emission hot spots are consistent with spatially aggregated 2D-rich domains, where excitonic confinement and energy funneling yield intensified radiative recombination. Notably, such electronic heterogeneity persists even when the surface topography appears comparable, highlighting the role of the ISC strategy in suppressing uncontrolled phase aggregation to achieve a more uniform interfacial environment. Conversely, the ISC-treated film maintains a uniform and intense emission without such segregation features. This confirms that the chemical reconstruction effectively immobilizes halide ions and suppresses the formation of iodide-rich traps. Although PL mapping reflects combined bulk and interfacial contributions, the improved PL stability is consistent with interfacial reconstruction, evidenced by KPFM homogenization and the elimination of unstable surface defect species identified by surface-sensitive spectroscopy. To quantify the carrier recombination kinetics, time-resolved PL (TRPL) measurements were performed on perovskite films deposited on the hole transport layer (Figure 2d). The decay curves were fitted with a tri-exponential function; a tri-exponential model was employed to capture the multi-component decay behavior typically observed in UWBG perovskites over the full temporal window, fitting details and the definition of average lifetime (τ_{avg}) are provided in Table S3. The control film shows a short τ_{avg} of 33.21 ns. This indicates that the majority of photogenerated carriers are rapidly annihilated via non-radiative recombination at the defective interface. The PEACl and EDA treatments yield comparable lifetimes of 30.46 ns and 36.82 ns, respectively, suggesting limited passivation effects. Strikingly, the ISC-treated film exhibits a significantly prolonged τ_{avg} of 129.20 ns. This nearly four-fold enhancement demonstrates that the ISC strategy effectively eliminates surface defects and suppresses interfacial non-radiative recombination losses, as supported by the concurrently homogenized surface CPD and the enhanced PL stability.

Photovoltaic hysteresis was evaluated for 2.0 eV single-junction devices configured in a p-i-n architecture. Figure 3a presents the *J-V* curves of the champion devices, and the detailed photovoltaic parameters are summarized in Table 2. The control device exhibits a limited PCE of 12.5% in the reverse scan, but it suffers from notable hysteresis, with the PCE dropping to 12.1% in the forward scan. This hysteresis is indicative of ion migration and charge accumulation at the defective perovskite/ETL interface. In stark contrast, the ISC-treated device achieves a champion PCE of 15.7% with negligible hysteresis (reverse PCE of 15.6%). Notably, the FF is significantly enhanced to 0.842, which is among the highest values reported for UWBG perovskite solar

16163028, 0, Downloaded from https://advanced.onlinelibrary.wiley.com/doi/10.1002/adfm.202532139 by Chungbuk National University, Wiley Online Library on [26/03/2026]. See the Terms and Conditions (https://onlinelibrary.wiley.com/terms-and-conditions) on Wiley Online Library for rules of use; OA articles are governed by the applicable Creative Commons License

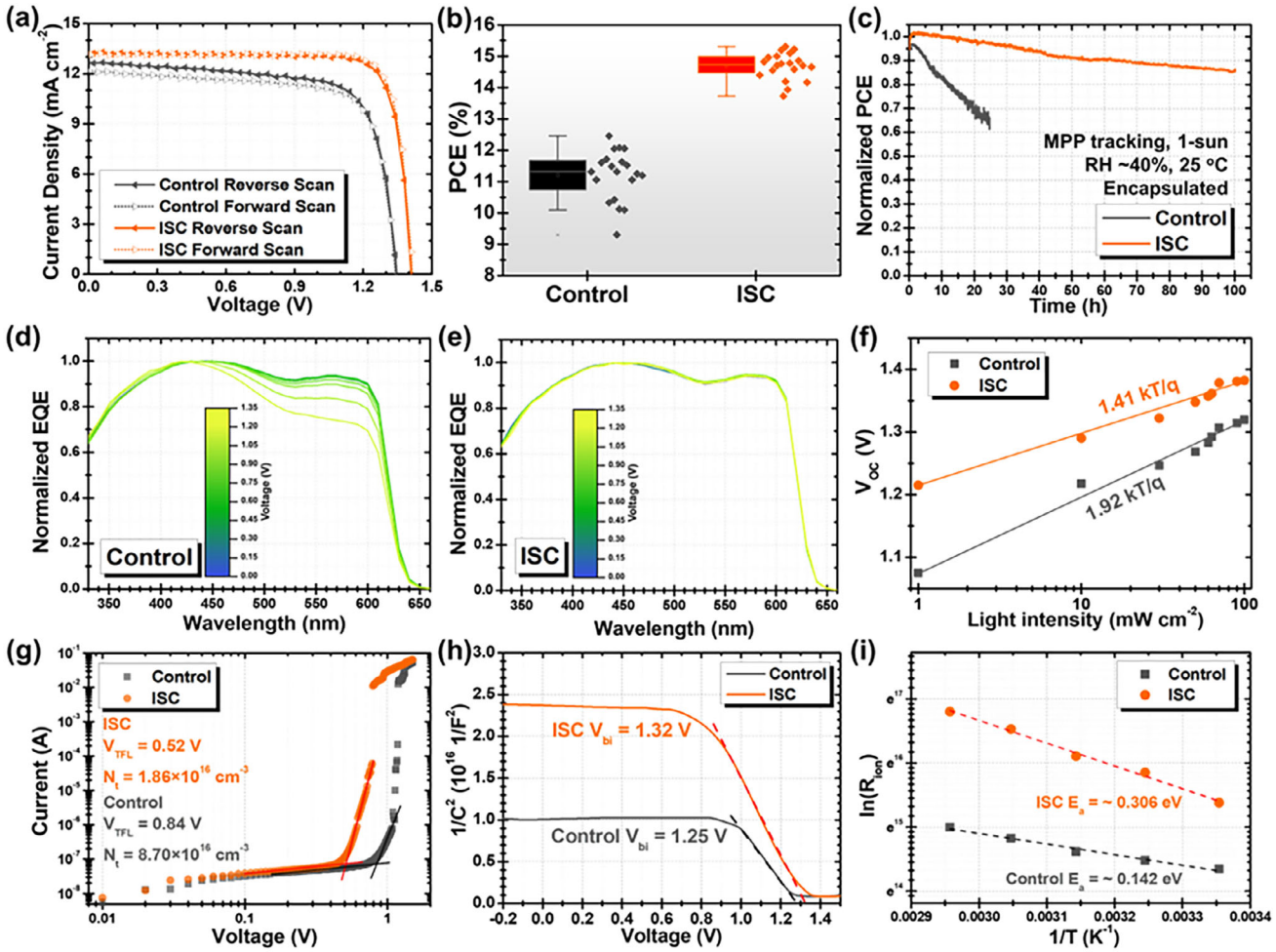

FIGURE 3 | (a) *J-V* curves of the champion Control and ISC-treated devices measured under reverse and forward scan directions. (b) Statistical distribution of PCE. (c) MPP tracking under continuous 1-sun illumination. Bias-dependent EQE spectra of (d) Control and (e) ISC devices and (f) Light-intensity dependence of V_{OC}. (g) SCLC analysis of electron-only devices with a configuration of ITO/SnO_x/perovskite/PCBM/BCP/Ag. (h) M-S plots and i) Arrhenius plots of R_{rec} derived from temperature-dependent EIS.

TABLE 2 | Photovoltaic parameters of the champion single-junction PSCs measured under forward and reverse scan directions. The average values and standard deviations were obtained from 20 independent devices.

	Scan direction	V_{OC} (V)	J_{SC} (mA cm^{-2})	FF	PCE (%)
Control champion	Forward	1.35	12.20	0.736	12.1
	Reverse	1.35	12.70	0.729	12.5
Control average		1.32 (±0.03)	12.11 (±0.39)	0.699 (±0.05)	11.2 (±0.8)
ISC champion	Forward	1.41	13.17	0.842	15.7
	Reverse	1.41	13.29	0.833	15.6
ISC average		1.40 (±0.01)	13.06 (±0.30)	0.801 (±0.03)	14.7 (±0.4)

cells. This improvement validates the formation of an Ohmic tunneling contact as predicted by the band diagram analysis. The statistical distribution of photovoltaic parameters, collected from 20 individual devices, is presented in Figure 3b and Figure S8. The ISC-treated devices show a narrow distribution in V_{OC}, J_{SC}, and FF compared to the control, demonstrating the high reproducibility of the chemical reconstruction strategy.

Long-term operational stability was assessed via maximum power point (MPP) tracking under continuous one-sun illumination in ambient air (Figure 3c). The encapsulated control device degrades rapidly, losing over 35% of its initial efficiency within 25 h. This degradation is typically associated with the photo-induced phase segregation of iodine-rich domains, which act as non-radiative recombination centers. Conversely, the ISC-treated device retains over 85% of its initial efficiency after 100 h.

16163028, 0, Downloaded from https://advanced.onlinelibrary.wiley.com/doi/10.1002/adfm.202532139 by Chungbuk National University, Wiley Online Library on [26/03/2026]. See the Terms and Conditions (https://onlinelibrary.wiley.com/terms-and-conditions) on Wiley Online Library for rules of use; OA articles are governed by the applicable Creative Commons License

This superior photostability corroborates the PL mapping results, confirming that the selective depletion of surface iodine and the immobilization of halides by the PEA-EDA complex effectively suppress the initiation of phase segregation.

To identify the dominant recombination pathway, bias-dependent external quantum efficiency (EQE) measurements were performed (Figure 3d,e). Recent drift-diffusion simulations suggest that the spectral evolution under forward bias acts as a fingerprint for locating recombination bottlenecks [34]. The control device exhibits a significant reduction in EQE magnitude under forward bias, specifically in the long-wavelength region (500–600 nm). Considering the p-i-n architecture, this spectral signature corresponds to a back-interface-limited recombination mechanism, confirming that the upper perovskite/ETL interface is the primary loss channel. On the other hand, the ISC-treated device maintains a robust EQE profile across the entire spectrum even under high forward bias. This signifies that novel surface engineering effectively eliminates the interfacial trap states, ensuring efficient carrier collection despite the reduced internal electric field.

Recombination kinetics were further quantified by analyzing the light-intensity dependence of V_{OC} (Figure 3f). The ideality factor (n) was extracted from the slope of the semi-logarithmic plot. The control device shows an ideality factor of 1.92, a value close to 2, which indicates that the device operation is dominated by trap-assisted Shockley-Read-Hall recombination [35, 36]. In comparison, the ISC-treated device exhibits a significantly reduced n value of 1.41. This decrease confirms the suppression of trap-mediated recombination, consistent with the prolonged carrier lifetime observed in TRPL.

The trap density was quantitatively determined using the space-charge-limited current (SCLC) method (Figure 3g). We fabricated electron-only devices with a configuration of ITO/SnO_x/perovskite/PCBM/BCP/Ag. The trap-filled limit voltage (V_{TFL}) decreases from 0.84 V for the control to 0.52 V for the ISC device. Accordingly, the calculated electron trap density (N_t) is reduced from 8.70×10^{16} cm^{-3} to 1.86×10^{16} cm^{-3}. This nearly five-fold reduction supports that the ISC treatment effectively passivates electron traps within the film.

To investigate the electrical properties of the junction, we conducted Mott-Schottky (M-S) analysis (Figure 3h). The ISC-treated device shows a higher built-in potential (V_{bi}) of 1.32 V compared to 1.25 V for the control. This enhancement aligns with the stronger downward band bending observed in UPS, confirming a more robust internal electric field for charge separation. Additionally, the slope of the linear region is steeper for the ISC device. Since the slope is inversely proportional to the carrier density, this indicates a reduction in the unintentional background doping density caused by charged defects.

Finally, ion migration kinetics were evaluated using temperature-dependent electrochemical impedance spectroscopy (EIS) (Figure 3i). The activation energy (E_a) for ion migration was derived from the Arrhenius plot of the recombination resistance (R_{rec}). The ISC-treated device exhibits a higher E_a of 0.306 eV compared to 0.142 eV for the control. This increased energy barrier confirms that the strong chemical anchoring of the ISC-derived amine complex effectively immobilizes the halide ions, thereby suppressing ion migration and enhancing the device stability against phase segregation [37, 38].

Driven by the reduced voltage deficit and enhanced photostability of the ISC-treated 2.0 eV devices, we fabricated monolithic all-perovskite 2-terminal (2T) tandem solar cells. Figure 4a illustrates the device architecture. The ISC-treated 2.0 eV UWBG perovskite serves as the top sub-cell. A 1.5 eV middle-bandgap (MBG) perovskite is utilized as the bottom sub-cell to maximize the spectral harvesting. An interconnection layer (ICL) consisting of sputtered IZO and atomic layer deposited (ALD) SnO_x connects the two sub-cells. This ICL facilitates efficient charge recombination without causing voltage loss. The photovoltaic performance of the tandem device and the corresponding single-junction sub-cells is presented in Figure 4b and summarized in Table 3. The single-junction top cell exhibits an open-circuit voltage V_{OC} of 1.41 V. The bottom cell shows a V_{OC} of 1.19 V with a PCE of 24.3%. Consequently, the champion tandem device achieves an exceptionally high V_{OC} of 2.58 V. This value corresponds to nearly the theoretical sum of the sub-cell voltages. It indicates that the ICL functions effectively with negligible voltage drop and that the high V_{OC} of the ISC-treated top cell is successfully translated into the tandem configuration.

Notably, achieving a V_{OC} of 2.58 V in a monolithic all-perovskite double-junction device represents one of the highest voltage outputs reported to date. This establishes a critical voltage benchmark for next-generation multijunction photovoltaics. Such high voltage headroom is significant because it relaxes voltage constraints in complex architectures. It enables rational extension toward perovskite/perovskite/Si or perovskite/perovskite/CIGS triple-junction configurations without severe cumulative voltage loss. In this context, the ISC-enabled UWBG top cell serves as a voltage-enabling platform. It elevates the achievable V_{OC} and overall efficiency potential of triple-junction solar cells.

The tandem device yields a J_{SC} of 11.90 mA cm^{-2} and an FF of 0.786. This results in a final PCE of 24.2%. Figure 4c displays the EQE spectra of the tandem device. The UWBG top cell absorbs the high-energy photons ($\lambda < 620$ nm). The MBG bottom cell harvests the transmitted low-energy photons (620 nm $< \lambda <$ 850 nm). The integrated currents calculated from the tandem EQE spectra show a close match. This signifies that the current mismatch loss is minimized. Additionally, the single-junction MBG bottom cell exhibits a high integrated J_{SC} of 23.9 mA cm^{-2} as shown in Figure S9. This confirms the high quality of the bottom absorber.

To contextualize our findings, we compared the V_{OC} of our tandem device with state-of-the-art WBG-based tandem solar cells reported in the literature (Figure S10), with detailed parameters provided in Table S4. Notably, a strictly matched comparison for two-junction tandems employing UWBG perovskite top cells (≈2.0 eV) remains limited at present, as such top cells have predominantly been explored in triple-junction architectures. Therefore, this comparison is provided for reference rather than as a direct ranking across disparate bandgap combinations and device configurations. In addition, for the 2.0 eV single-junction devices, ISC increases V_{OC} from 1.35 to 1.41 V, corresponding to a reduced V_{loss} ($E_g/q - V_{OC}$) from 0.65 to 0.59 V. Taken

16163028, 0, Downloaded from https://advanced.onlinelibrary.wiley.com/doi/10.1002/adfm.202532139 by Chungbuk National University, Wiley Online Library on [26/03/2026]. See the Terms and Conditions (https://onlinelibrary.wiley.com/terms-and-conditions) on Wiley Online Library for rules of use; OA articles are governed by the applicable Creative Commons License

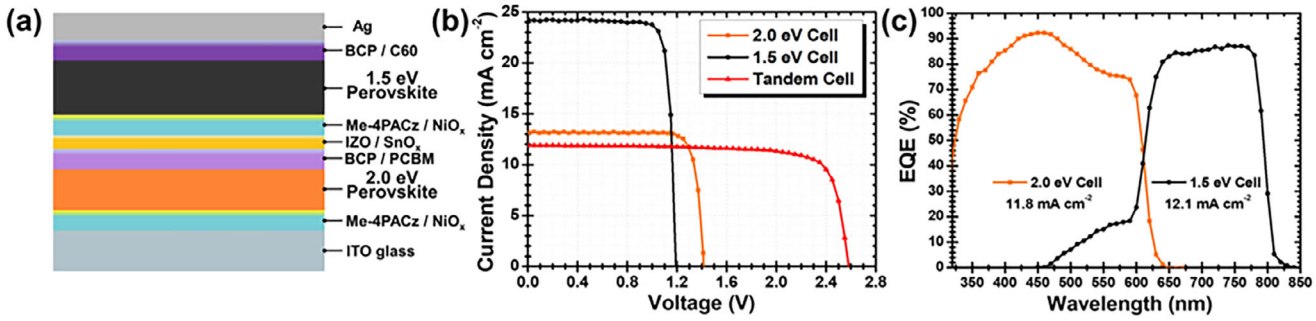

FIGURE 4 | (a) Schematic architecture of the monolithic tandem device utilizing the ISC-treated 2.0 eV perovskite as the top cell. (b) *J-V* characteristics of the single-junction top (2.0 eV), bottom (1.5 eV), and the 2T tandem device. (c) EQE spectra of the top and bottom sub-cells in the tandem device.

TABLE 3 | Photovoltaic parameters of the single-junction sub-cells (2.0 eV Top, 1.5 eV Bottom) and the monolithic tandem solar cell.

Device	V_{OC} (V)	J_{SC} (mA cm^{-2})	FF	PCE (%)
2.0 eV	1.41	13.17	0.842	15.7
1.5 eV	1.19	24.31	0.840	24.3
Tandem	2.58	11.90	0.786	24.2

together, these results demonstrate that the ISC strategy provides a robust and scalable pathway for voltage-centric device design, positioning it as a key enabler for the performance escalation of triple-junction solar cells.

3 | Conclusion

In summary, we demonstrate an ISC strategy to overcome the performance bottlenecks of 2.0 eV UWBG perovskite solar cells. We reveal that the in situ proton transfer reaction between PEACl and EDA activates the amine precursors, facilitating the formation of a molecularly ordered passivation layer and eliminating surface metallic defects. Comprehensive UPS and KPFM analyses confirm that this reconstruction induces a degenerate-like n-type surface character, which is confined to the near-surface region and is functionally relevant for tunneling-enabled electron extraction rather than bulk electronic doping. This energetic alignment creates a robust hole-blocking barrier and enables efficient electron extraction via an Ohmic tunneling contact. As a result, the single-junction device achieves a PCE of 15.7% with a high FF and improved operational stability against phase segregation. Finally, we realize a monolithic all-perovskite tandem solar cell delivering a PCE of 24.2% with a high V_{OC} of 2.58 V, establishing a new voltage benchmark for perovskite-based multijunction photovoltaics. Importantly, the demonstrated surface-energetics engineering of the 2.0/1.5 eV perovskite subcells provides a key technological foundation for extending perovskite tandems toward perovskite/perovskite/Si triple-junction architecture, where ultrahigh voltage and interfacial phase stability are critical. This work therefore offers a fundamental pathway to optimizing interfacial energetics and accelerating the development of high-efficiency, stable multijunction photovoltaics.

4 | Experimental Section

4.1 | Materials

Nickel(II) nitrate hexahydrate ($Ni(NO_3)_2$•$6H_2O$), ethylenediamine (EDA), lead(II) bromide ($PbBr_2$), lead(II) chloride ($PbCl_2$), and methylammonium chloride (MACl) were purchased from Sigma–Aldrich. Ethylene glycol (EG), N,N-dimethylformamide (DMF), dimethyl sulfoxide (DMSO), isopropyl alcohol (IPA), and toluene were purchased from Samchun Chemical. Chlorobenzene (CB) was purchased from Kanto Chemical. Cesium iodide (CsI) was purchased from Alfa Aesar. Formamidinium iodide (FAI), phenethylammonium chloride (PEACl), and methylammonium iodide (MAI) were obtained from Greatcell Solar Materials. Lead(II) iodide (PbI_2) and [4-(3,6-Dimethyl-9H-carbazol-9-yl)butyl]phosphonic acid (Me-4PACz) were purchased from TCI. [6,6]-Phenyl-C61-butyric acid methyl ester ($PC_{61}BM$), fullerene (C_{60}), and bathocuproine (BCP) were purchased from OSM. NiO_x nanoparticle ink was purchased from Avantama. Patterned indium tin oxide (ITO) coated glass substrates (10 Ω sq^{-1}) were purchased from AMGlass. All materials were used as received without further purification.

4.2 | Fabrication of 2.0 eV Single-Junction PSCs

The 2.0 eV UWBG perovskite solar cells were fabricated with an inverted p-i-n configuration of ITO/NiO_x (sol-gel)/Me-4PACz/Perovskite/Surface Treatment/PCBM/BCP/Ag. Patterned ITO substrates were sequentially cleaned by sonication in acetone and IPA for 20 min each, dried at 95°C, and treated with UV-ozone for 30 min. The NiO_x sol-gel precursor (0.2 M) was prepared by dissolving nickel nitrate hexahydrate (0.2 mol) and EDA (0.2 mol) in EG (1 mL). This solution was spin-coated onto the ITO substrates at 5000 rpm for 30 s, followed by annealing at 150°C for 5 min and 300°C for 60 min in air. After transferring to an N_2-filled glovebox, a Me-4PACz solution (0.5 mg mL^{-1} in EtOH) was deposited onto the NiO_x layer, held for 15 s, spin-coated at 3000 rpm for 30 s, and annealed at 125°C for 10 min. The 1 M UWBG perovskite precursor $FA_{0.85}Cs_{0.15}PbIBr_{1.8}Cl_{0.2}$ was prepared by dissolving FAI (0.85 mol), CsI (0.15 mol), $PbBr_2$ (0.9 mol), and $PbCl_2$ (0.1 mol) in a DMF:DMSO mixed solvent (7:3 v/v) with 1.5 mol% urea additive. The solution was stirred at 70°C for 2 h. The precursor was spin-coated using a two-step program: 1000 rpm for 10 s (ramp 5 s) and 6000 rpm for 45 s (ramp 2.5 s).

16163028, 0, Downloaded from https://advanced.onlinelibrary.wiley.com/doi/10.1002/adfm.202532139 by Chungbuk National University, Wiley Online Library on [26/03/2026]. See the Terms and Conditions (https://onlinelibrary.wiley.com/terms-and-conditions) on Wiley Online Library for rules of use; OA articles are governed by the applicable Creative Commons License

Diethyl ether (0.4 mL) was dripped onto the spinning substrate 28 s after the start. The films were annealed at 70°C for 2 min and then at 100°C for 10 min. For the ISC treatment, a mixed solution of PEACl (1.0 mg mL^{-1} in IPA) and EDA (3 mM in toluene) (1:1 v/v) was dynamically spin-coated at 6000 rpm for 20 s, followed by annealing at 70°C for 5 min. Subsequently, a PCBM solution (20 mg mL^{-1} in chlorobenzene) was spin-coated at 1500 rpm for 25 s and annealed at 100°C for 5 min. A BCP solution (0.5 mg mL^{-1} in IPA) was then dynamically spin-coated at 4000 rpm for 20 s. Finally, a 150 nm thick Ag electrode was deposited by thermal evaporation. The active area of the device was 6.25 mm^2.

4.3 | Fabrication of 1.5 eV Single-Junction PSCs

The 1.5 eV MBG perovskite solar cells were fabricated with a structure of ITO/NiO_x (nanoparticle)/Me-4PACz/Perovskite/$PDAI_2$/C_{60}/BCP/Ag. The commercial NiO_x nanoparticle ink was diluted with IPA (1:9 v/v) and spin-coated onto cleaned ITO substrates at 3000 rpm for 30 s in ambient air, followed by annealing at 150°C for 20 min. The 1.5 M MBG perovskite precursor $Cs_{0.05}MA_{0.10}FA_{0.85}PbI_3$ was prepared by dissolving CsI (0.05 mol), MAI (0.1 mol), FAI (0.85 mol), PbI_2 (1.10 mol), and MACl (0.1 mol, additive) in a DMF:DMSO mixed solvent (4:1 v/v, 0.8 mL:0.2 mL). The solution was vortexed overnight before use. In a N_2-filled glovebox, the perovskite precursor was spin-coated onto the Me-4PACz layer at 1000 rpm for 10 s followed by 6000 rpm for 40 s. Anisole (0.3 mL) was dripped 15 s before the end of the program. The films were annealed at 100°C for 20 min. A $PDAI_2$ solution (0.5 mg mL^{-1} in IPA) was spin-coated at 4000 rpm for 30 s and annealed at 100°C for 5 min. Subsequently, a 20 nm thick C_{60} layer was deposited by thermal evaporation at a rate of 0.1 Å s^{-1}. The BCP layer and Ag electrode were deposited using the same procedures as for the 2.0 eV devices.

4.4 | Fabrication of Monolithic All-Perovskite (2T) Tandem Solar Cell

First, the 2.0 eV WBG top cell was fabricated on the patterned ITO substrate following the same procedure as the single-junction devices, up to the PCBM/BCP layer. Subsequently, an ICL consisting of SnO_x/IZO was then deposited. A 20 nm thick SnOx layer was deposited by atomic layer deposition (ALD, Lucida D200, NCD) using tetrakis(dimethylamino)tin(IV) (TDMASn) as the precursor at 100°C. Subsequently, a 3 nm thick indium zinc oxide (IZO) layer was deposited by RF magnetron sputtering at 100 W power. The 1.5 eV bottom cell, including the NiO_x/Me-4PACz HTL, perovskite absorber with $PDAI_2$ treatment, and ETLs, was then fabricated on top of the ICL using the same procedures as the single-junction devices. Finally, a 150 nm Ag top electrode was thermally evaporated.

4.5 | Characterization

The *J-V* characteristics were measured using a Keithley 2400 source meter under simulated AM 1.5G illumination (100 mW cm^{-2}) from a solar simulator. The light intensity was calibrated using a standard silicon reference cell. MPPT was conducted using an LED solar simulator (Newport, LSH-7320), calibrated with a silicon photodiode detector (BS-500BK, BUNKOUKEIKI CO., LTD.). MPPT measurements were performed using a Keithley 2400 source meter. EQE was measured using the QuantX-300 QE measurement system (Newport). For tandem subcell EQE measurements, bias illumination was applied to the complementary subcell to avoid current-limitation: a green LED source (centered at 520 nm, FWHM about 30 nm) was used as bias light when measuring the bottom subcell EQE, whereas an NIR LED source (centered at 750 nm, FWHM about 30 nm) was used as bias light when measuring the top subcell EQE. A metal aperture mask with an area of 0.04 cm^2 was used for all measurements. The surface morphology and roughness were characterized by AFM and KPFM using an Oxford Instruments MFP-3D Origin+ system. To visualize the phase segregation and homogeneity, PL mapping was performed using an Olympus BX53F2 microscope equipped with cellSens software. TRPL decay kinetics were measured using an Edinburgh Instruments FLS1000 fluorescence spectrometer. Crystal structures were analyzed by XRD, Bruker D8 Advance with Cu Kα radiation. Chemical states were investigated using XPS, Thermo Scientific K-Alpha, and UPS, Thermo Fisher Scientific Nexsa with a He I UV source (21.22 eV).

Acknowledgements

This work was supported by the National Research Foundation of Korea (NRF) grant funded by the Korea government (MSIT) (NRF—RS-2023-00212744, RS-2023-00217270, RS-2024-00436187).

Funding

This work was supported by the National Research Foundation of Korea (NRF) grant funded by the Korea government (MSIT) (NRF – RS-2023-00212744, RS-2023-00217270, RS-2024-00436187).

Conflicts of Interest

The authors declare no conflict of interest.

Data Availability Statement

The data that support the findings of this study are available from the corresponding author upon reasonable request.;

References

1. Y. Yang, H. Chen, C. Liu, et al., "Amidination of Ligands for Chemical and Field-effect Passivation Stabilizes Perovskite Solar Cells," *Science* 384, no. 6698 (2024): 898–902.

2. H. Chen, C. Liu, J. Xu, et al., "Homogeneous Crystallization and Buried Interface Passivation for Perovskite Tandem Solar Modules," *Science* 383, no. 6692 (2024): 855–859, https://doi.org/10.1126/science.adj6088.

3. J. Y. Jiang, "Environmental Fatigue Crack Growth of PV glass/EVA Laminates in the Melting Range," *Progress in Photovoltaics: Research and Applications* 32, no. 1 (2025): 623–635, https://doi.org/10.1002/pip.3800.

4. M. Heydarian, M. Heydarian, P. Schygulla, et al., "Recent Progress in Monolithic Two-Terminal Perovskite-Based Triple-Junction Solar Cells," *Energy & Environmental Science* 17, no. 4 (2024): 1781–1818, https://doi.org/10.1039/d3ee02822d.

5. L. Duan, X. Cui, C. Xu, Z. Chen, and J. Zheng, "Monolithic Perovskite/Perovskite/Silicon Triple-Junction Solar Cells: Fundamentals, Progress, and Prospects," *Nano-Micro Letters* 18 (2025): 8, https://doi.org/10.1007/s40820-025-01836-8.

16163028, 0, Downloaded from https://advanced.onlinelibrary.wiley.com/doi/10.1002/adfm.202532139 by Chungbuk National University, Wiley Online Library on [26/03/2026]. See the Terms and Conditions (https://onlinelibrary.wiley.com/terms-and-conditions) on Wiley Online Library for rules of use; OA articles are governed by the applicable Creative Commons License

6. J. Mei and F. Yan, "Recent Advances in Wide-Bandgap Perovskite Solar Cells," *Advanced Materials* 37 (2025): 2418622, https://doi.org/10.1002/adma.202418622.

7. J. Wang, L. Zeng, D. Zhang, et al., "Halide Homogenization for Low Energy Loss in 2-eV-bandgap Perovskites and Increased Efficiency in all-perovskite Triple-junction Solar Cells," *Nature Energy* 9 (2023): 70–80, https://doi.org/10.1038/s41560-023-01406-5.

8. Z. Wang, L. Zeng, T. Zhu, et al., "Suppressed Phase Segregation for Triple-junction Perovskite Solar Cells," *Nature* 618, no. 7963 (2023): 74–79, https://doi.org/10.1038/s41586-023-06006-7.

9. F. Li, D. Wu, L. Shang, et al., "Highly Efficient Monolithic Perovskite/Perovskite/Silicon Triple-Junction Solar Cells," *Advanced Materials* 36, no. 14 (2024): 2311595, https://doi.org/10.1002/adma.202311595.

10. S. Liu, Y. Lu, C. Yu, et al., "Triple-Junction Solar Cells With Cyanate in Ultrawide-bandgap Perovskites," *Nature* 628, no. 8011 (2024): 306–312, https://doi.org/10.1038/s41586-024-07226-1.

11. T. Ye, L. Qiao, T. Wang, et al., "Molecular Synergistic Effect for High Efficiency Monolithic Perovskite/Perovskite/Silicon Triple-Junction Tandem Solar Cells," *Advanced Energy Materials* 14 (2024): 2402491, https://doi.org/10.1002/aenm.20240249112.

12. Z. Liu, R. Lin, M. Wei, et al., "All-Perovskite Tandem Solar Cells Achieving >29% Efficiency With Improved (100) Orientation in Wide-Bandgap Perovskites," *Nature Materials* 24 (2025): 252–259, https://doi.org/10.1038/s41563-024-02073-x.

13. Z. Xu, J. Han, G. Li, et al., "Halide-mixing Braking Strategy for 1.95 eV Wide-Bandgap Perovskites Enabling High-efficiency Triple-Junction Tandems," *Energy & Environmental Science* 19 (2025): 221–229, https://doi.org/10.1039/d5ee05574a.

14. Z. Chen, K. Ren, S. Yue, C. Li, and Z. Fang, "Performance-Enhancing Strategies for Wide-Bandgap Perovskite Solar Cells and Their Tandem Applications," 10, no. 2 (2025): 6500, https://doi.org/10.1021/acsenergylett.4c03123.

15. Y. Guo, H. Tan, and B. Xu, "Concurrent Electrode–Electrolyte Interfaces Engineering via Nano-Si 3 N 4 Additive for High-Rate, High-Voltage Lithium Metal Batteries," *Energy & Environmental Science* 18 (2025): 3148–3159, https://doi.org/10.1039/D4EE03862B.

16. G. Xie, H. Li, J. Fang, et al., "Crystallization Thermodynamics Regulation of 1.85 eV Wide-Bandgap Perovskite for Efficient and Stable Perovskite-Organic Tandem Photovoltaics," *Angewandte Chemie International Edition* 64 (2025): 202501764, https://doi.org/10.1002/anie.202501764.

17. X. Li, S. Aftab, S. Hussain, et al., "Dimensional Diversity (0D, 1D, 2D, and 3D) in Perovskite Solar Cells: Exploring the Potential of Mixed-dimensional Integrations," *Journal of Materials Chemistry A* 12 (2024): 4421–4440, https://doi.org/10.1039/d3ta07663f.

18. A. S. Bati, M. Batmunkh, and J. G. Shapter, "Emerging 2D Layered Materials for Perovskite Solar Cells," *Advanced Energy Materials* 10, no. 9 (2020): 1902253, https://doi.org/10.1002/aenm.201902253.

19. A. Krishna, S. Gottis, M. K. Nazeeruddin, and F. Sauvage, "Mixed Dimensional 2D/3D Hybrid Perovskite Absorbers: The Future of Perovskite Solar Cells?," *Advanced Functional Materials* 29, no. 8 (2019): 1806482, https://doi.org/10.1002/adfm.201806482.

20. Y. Zhou, X. Zhang, Z. Feng, et al., "Penetrative and Homogenized Surface Passivation for Evaporation-Solution-Processed Perovskite Solar Cells via a Synergistic Bimolecular Strategy," *Advanced Functional Materials* 35 (2025): 2424070, https://doi.org/10.1002/adfm.202424070.

21. Z. Xu, N. Liu, X. Liu, et al., "Multifunctional Alkylamines Enable Defect Passivation and Energy Level Alignment for Efficient and Stable Inverted $CsPbI_3$ Perovskite Solar Cells," *Chemical Engineering Journal* 451 (2023): 139047, https://doi.org/10.1016/j.cej.2022.139047.

22. M. Taddei, J. A. Smith, B. M. Gallant, et al., "Ethylenediamine Addition Improves Performance and Suppresses Phase Instabilities in Mixed-halide Perovskites," *ACS Energy Letters* 7, no. 12 (2022): 4265–4273, https://doi.org/10.1021/acsenergylett.2c02113.

23. S. Senra-Ferreiro, F. Pena-Pereira, I. Costas-Mora, V. Romero, I. Lavilla, and C. Bendicho, "Comparison of Different Extraction Methods for the Determination of Statin Drugs in Wastewater and River Water by HPLC/Q-TOF-MS," *Talanta* 85, no. 5 (2011): 607–615, https://doi.org/10.1016/j.talanta.2011.04.017.

24. V. M. Egorov, S. V. Smirnova, and I. V. Pletnev, "Performance of a Nitrifying Airlift Reactor Using Granular Sludge," *Separation and Purification Technology* 63, no. 3 (2008): 670–675, https://doi.org/10.1016/j.seppur.2008.07.012.

25. T. Mizutani, H. Takagi, Y. Ueno, T. Horiguchi, K. Yamamura, and H. Ogoshi, "Hydrogen-Bonding-Based Thermochromic Phenol–Amine Complexes," *Journal of Physical Organic Chemistry* 11, no. 10 (1998): 737–742, https://doi.org/10.1002/(SICI)1099-1395(1998100)11.

26. W. Fu, H. Liu, X. Shi, L. Zuo, X. Li, and A. K. Y. Jen, "Tailoring the Functionality of Organic Spacer Cations for Efficient and Stable Quasi-2D Perovskite Solar Cells," *Advanced Functional Materials* 29, no. 38 (2019): 1900221, https://doi.org/10.1002/adfm.201900221.

27. K. Lee, J. Kim, H. Yu, et al., "A Highly Stable and Efficient Carbon Electrode-based Perovskite Solar Cell Achieved via Interfacial Growth of 2D PEA_2PbI_4 Perovskite," *Journal of Materials Chemistry A* 6 (2018): 24560–24568, https://doi.org/10.1039/c8ta08569c.

28. J. Liang, X. Hu, C. Wang, et al., "Ammonia Eurefstics: Electrolytes for Liquid Energy Storage and Conversion at Room Temperature and Ambient Pressure," *Joule* 6, no. 4 (2022): 772–781, https://doi.org/10.1016/j.joule.2022.03.001.

29. W.-C. Lin, W.-C. Lo, J.-X. Li, Y.-K. Wang, J.-F. Tang, and Z.-Y. Fong, "In Situ XPS Investigation of the X-Ray-Triggered Decomposition of Perovskites in Ultrahigh Vacuum Condition," *Materials Degradation* 5 (2021): 13, https://doi.org/10.1038/s41529-021-00160-w.

30. J. Hu, R. A. Kerner, I. Pelczer, B. P. Rand, and J. Schwartz, "Organoammonium-Ion-based Perovskites Can Degrade to Pb0 via Amine–Pb (II) Coordination," *ACS Energy Letters* 6, no. 7 (2021): 2262–2267, https://doi.org/10.1021/acsenergylett.1c00828.

31. Z. Liu, H. Li, Z. Chu, et al., "Reducing Perovskite/C 60 Interface Losses via Sequential Interface Engineering for Efficient Perovskite/Silicon Tandem Solar Cell," *Advanced Materials* 36, no. 9 (2024): 2308370, https://doi.org/10.1002/adma.202308370.

32. Y. Guo, C. Zhang, L. Wang, et al., "Unveiling the Impact of Photoinduced Halide Segregation on Performance Degradation in Wide-bandgap Perovskite Solar Cells," *Energy & Environmental Science* 18 (2025): 2308–2317, https://doi.org/10.1039/d4ee03859b.

33. X. Lian, Y. Xu, W. Fu, et al., "Homogenizing Morphology and Composition of Methylammonium-Free Wide-Bandgap Perovskite for Efficient and Stable Tandem Solar Cells," *Advanced Functional Materials* 34, no. 31 (2024): 2402061, https://doi.org/10.1002/adfm.202402061.

34. A. Abudulimu, S. L. Wenner, A. B. Phillips, et al., "Bias-Dependent Quantum Efficiency Reveals Recombination Pathways in Thin Film Solar Cells," *Advanced Energy Materials* 15 (2025): 2501709, https://doi.org/10.1002/aenm.202501709.

35. S. Ryu, N. Y. Ha, Y. Ahn, J.-Y. Park, and S. Lee, "Light Intensity Dependence of Organic Solar Cell Operation and Dominance Switching Between Shockley–Read–Hall and Bimolecular Recombination Losses," *Scientific Reports* 11 (2021): 16781, https://doi.org/10.1038/s41598-021-96336-x.

36. N. Thongprong, T. Supasai, Y. Li, I.-M. Tang, and N. Rujisamphan, "Insights Into Recombination Processes From Light Intensity–Dependent Open-Circuit Voltages and Ideality Factors in Planar Perovskite Solar Cells," *Energy Technology* 8, no. 1 (2020): 1901196, https://doi.org/10.1002/ente.201901196.

37. A. Keefe, S. Buteau, I. Hill, and J. Dahn, "Thermodynamically Consistent and Computationally Efficient 0D Lithium Intercalation Model of a Phase Separating Cathode Particle," *Journal of The Electrochem-*

16163028, 0, Downloaded from https://advanced.onlinelibrary.wiley.com/doi/10.1002/adfm.202532139 by Chungbuk National University, Wiley Online Library on [26/03/2026]. See the Terms and Conditions (https://onlinelibrary.wiley.com/terms-and-conditions) on Wiley Online Library for rules of use; OA articles are governed by the applicable Creative Commons License

ical Society 166, no. 14 (2019): A3242–A3249, https://doi.org/10.1149/2.0381914jes.

38. B. Y. Liaw, E. P. Roth, R. G. Jungst, G. Nagasubramanian, H. L. Case, and D. H. Doughty, "Correlation of Arrhenius Behaviors in Power and Capacity Fades With Cell Impedance and Heat Generation in Cylindrical Lithium-ion Cells," *Journal of Power Sources* 119–121 (2003): 874–886, https://doi.org/10.1016/S0378-7753(03)00298-3.

Supporting Information

Additional supporting information can be found online in the Supporting Information section.

Supporting File 1: adfm75076-sup-0001-SuppMat.docx.

Supporting File 2: adfm75076-sup-0002-Data.zip.

16163028, 0, Downloaded from https://advanced.onlinelibrary.wiley.com/doi/10.1002/adfm.202532139 by Chungbuk National University, Wiley Online Library on [26/03/2026]. See the Terms and Conditions (https://onlinelibrary.wiley.com/terms-and-conditions) on Wiley Online Library for rules of use; OA articles are governed by the applicable Creative Commons License